

Quantifying and Understanding the Tilt of a Pt Janus Active Colloid Near Solid Walls

Jiayu Liu^{1#}, Yankai Xu^{2#}, Zihan Qiao¹, Shanshan Li³, Xing Ma^{3, 4}, Ting Kuang⁵, H. P. Zhang^{2*}, Wei Wang^{1*}

1 School of Materials Science and Engineering, Harbin Institute of Technology (Shenzhen), Shenzhen, China, 518055

2 School of Physics and Astronomy, Institute of Natural Sciences and MOE-LSC, Shanghai Jiao Tong University, Shanghai 200240, China

3 School of Integrated Circuits, Harbin Institute of Technology (Shenzhen), Shenzhen 518055, China

4 Sauvage Laboratory for Smart Materials, School of Materials Science and Engineering, Harbin Institute of Technology (Shenzhen), Shenzhen 518055, China

5 Education Center of Experiments and Innovations, Harbin Institute of Technology (Shenzhen), Shenzhen, China, 518055

Contact author: weiwangsz@hit.edu.cn

Contact author: hepeng_zhang@sjtu.edu.cn

#: authors contributed equally

I. EXPERIMENTS

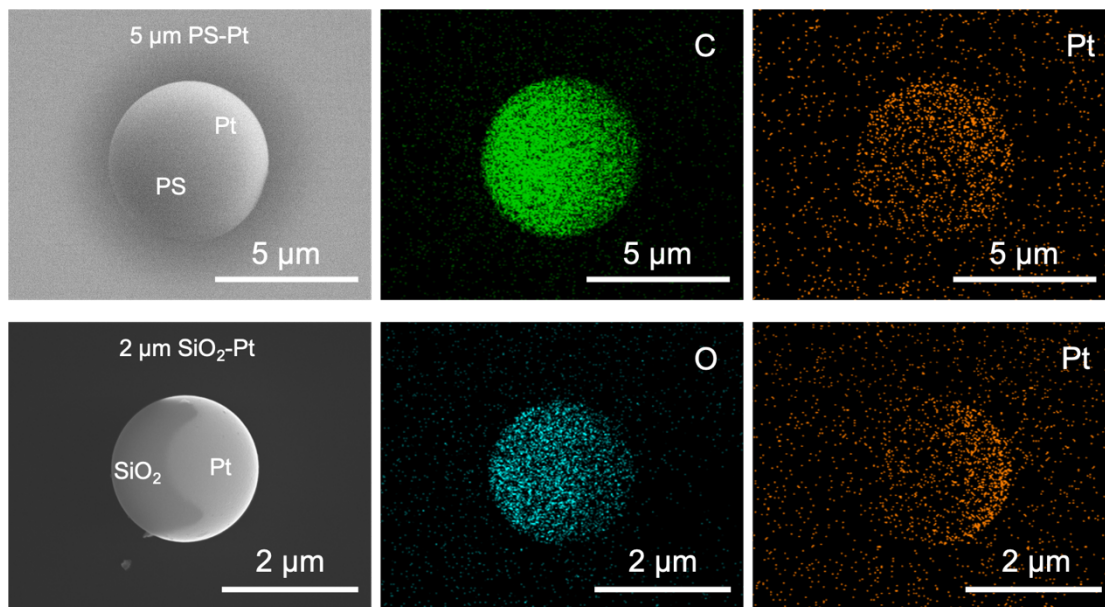


Figure S1. SEM and EDS mapping of 5 μm PS-Pt and 2 μm SiO₂-Pt Janus microspheres.

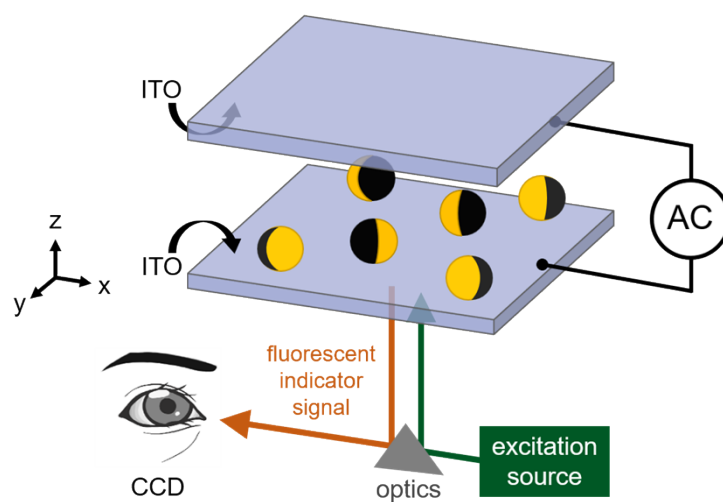


Figure S2. Schematic diagram of the experimental chamber with Janus Pt colloids sandwiched between two pieces of ITOs.

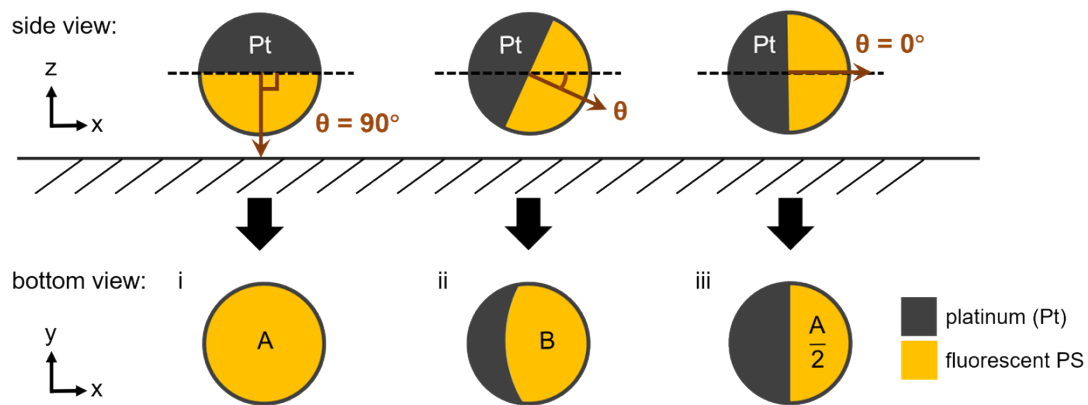


Figure S3. Schematic illustration of the moon phases and corresponding tilt angles of Janus Pt colloids: i) side and bottom view of a Janus motor with tilt angle $\theta = 90^\circ$, ii) side and bottom view of a Janus motor with a non-zero θ , iii) side and bottom view of a Janus motor with $\theta = 0^\circ$, which is experimentally realized by the application of a vertical electric field.

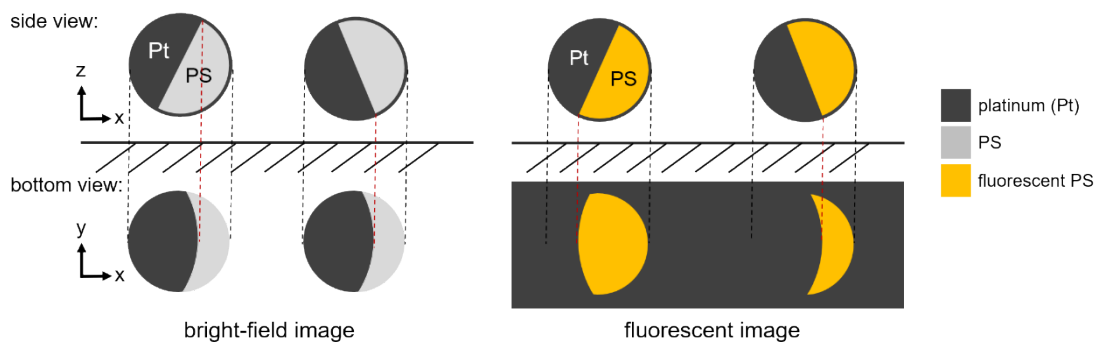


Figure S4. Schematic illustration of the differences of the moon phases of Janus Pt colloids acquired by bright-field microscopy (left) and epi fluorescence microscopy (right). Note how bright field images cannot distinguish between the two configurations.

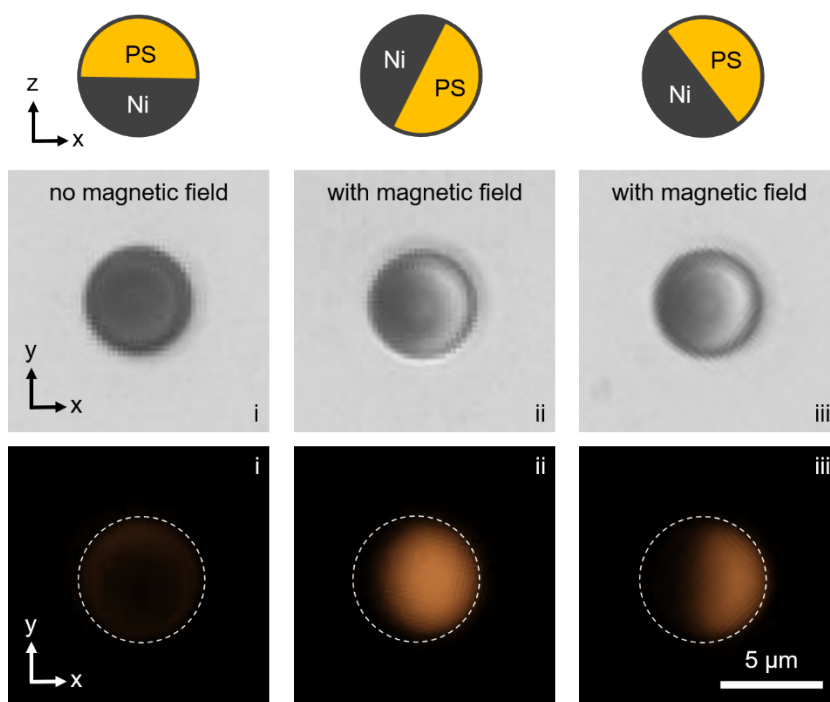


Figure S5. The differences in the optical micrographs of 5 μm Janus PS-Ni colloids acquired by bright-field microscopy (center row) and epi fluorescent microscopy (bottom row). A handheld magnet was used to tilt the Janus sphere.

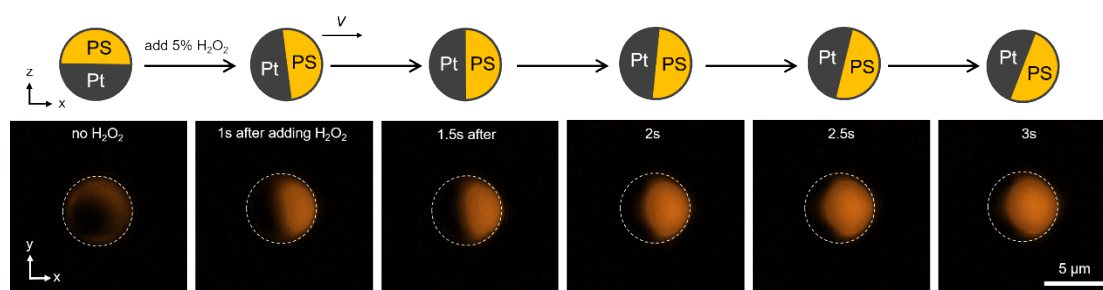


Figure S6. A 5 μm PS-Pt colloid gradually flipped and started to move after the addition of 5% H_2O_2 , with 10 nm Pt cap.

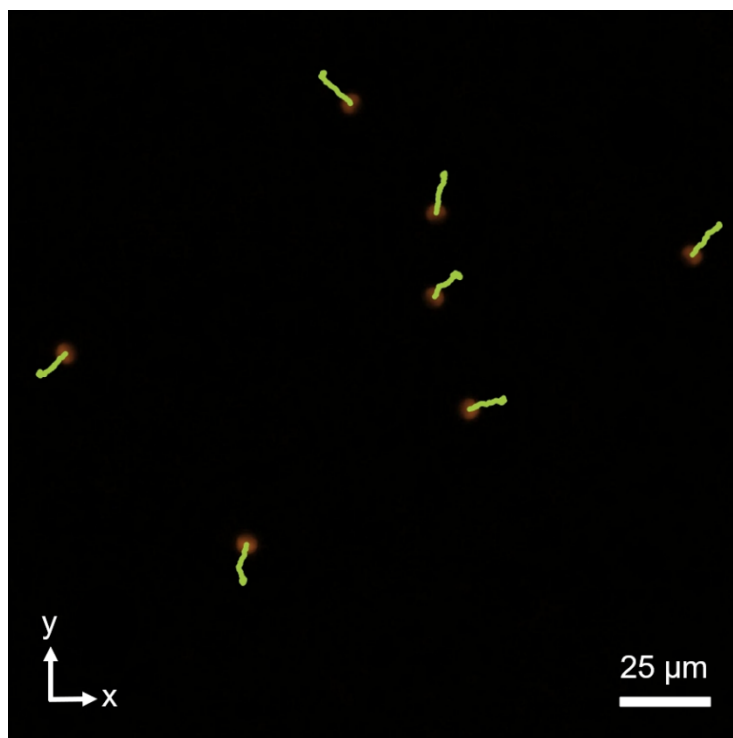


Figure S7. 10 s trajectory of 5 μm Janus PS-Pt colloids in 5% H_2O_2 , under a sinusoidal AC electric field of 1 MHz and a time averaged electric field strength of 17.7 V/mm .

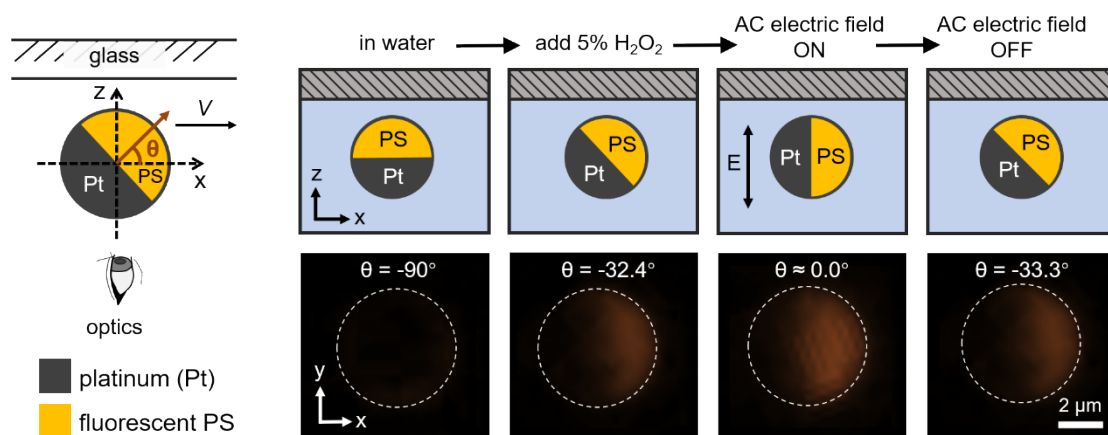


Figure S8. Quantifying the θ of a 5 μm PS-Pt Janus active colloid moving along a top ceiling in 5% H_2O_2 . The colloid was coated with 10 nm Pt cap.

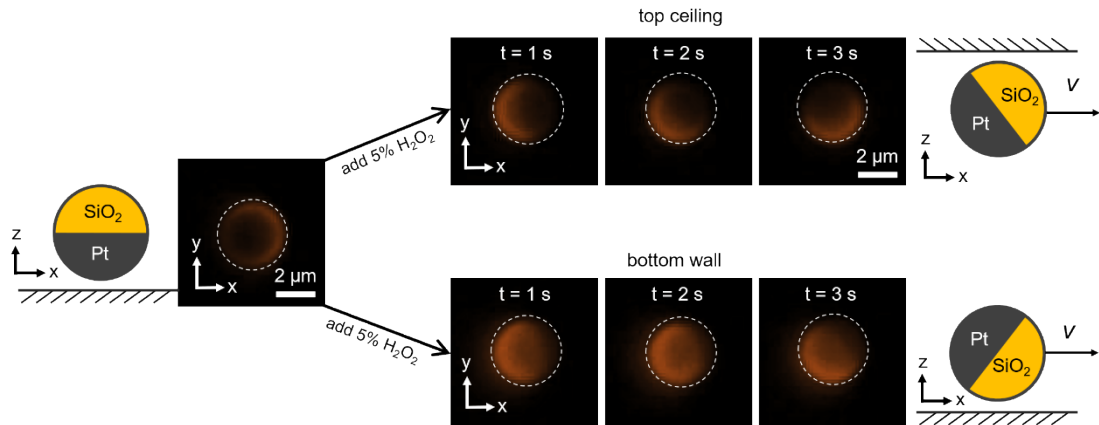


Figure S9. Fluorescence imaging of SiO₂-Pt Janus colloids moving in 5% H₂O₂ along the bottom wall and top ceiling. The colloid was coated with 10 nm Pt cap.

II. NUMERICAL METHODS

Based on our previous research^[1], we apply the finite element method to solve the Poisson-Nernst-Planck-Stokes equations with fully resolved electric double layers. The 2D model is computed within a $160\ \mu\text{m}$ by $80\ \mu\text{m}$ domain in the x - z plane, as depicted in Figure S10. When 5% H_2O_2 triggers chemical reactions on the motor surface, we assume that the proton fluxes on the anode and cathode hemispheres are in opposite directions, resulting in a net ion flux of zero. Protons are generated at the equator of the Pt side (anode) and absorbed at the poles of the Pt side (cathode),^[2] as shown in Figure S11. The charged wall disturbs the upper and lower equilibrium of the physical fields generated by the motor.

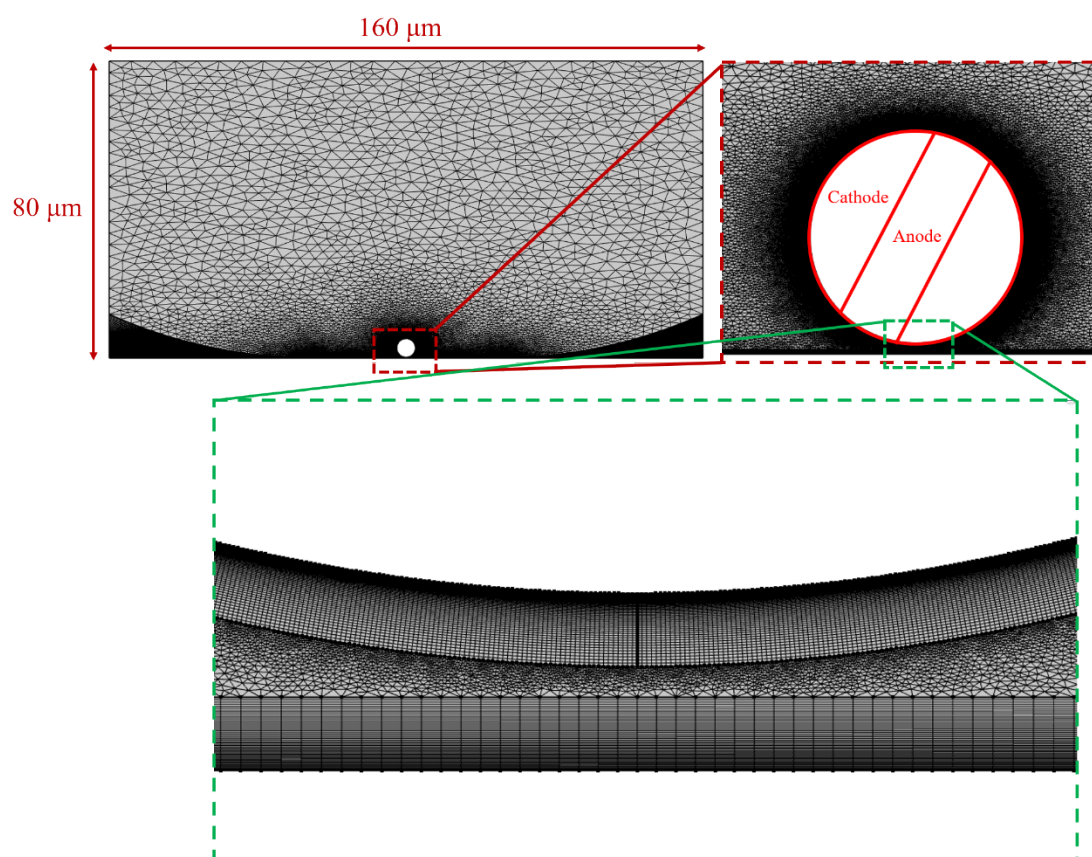


Figure S10. Schematic of the geometric setup of the model

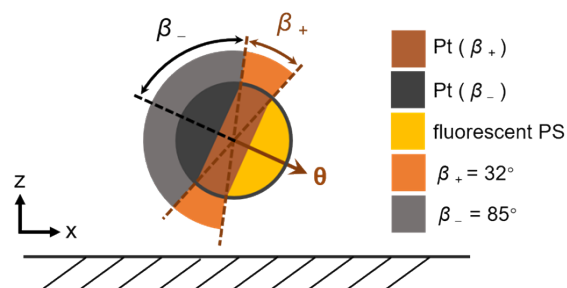


Figure S11. Schematic of the model β range setting

Our model accounts for an electrolyte containing equal concentrations of H^+ and OH^- ions, along with background ions, denoted as BI^+ and BI^- , which are included to modify the ionic strength and Debye length. With the Debye length set to 70 nm, the equilibrium height of the motors is approximately 0.27 μm , aligning closely with the experimentally measured equilibrium height.^[3]

In the limit of dilute solutions, the steady-state ion concentration distribution c_i for the i -th ion is governed by the Nernst-Planck equation:

$$\nabla \cdot \mathbf{J}_i = 0 \quad (1)$$

$$\mathbf{J}_i = -D_i \nabla c_i - z_i F v_i c_i \nabla \phi \quad (2)$$

where \mathbf{J}_i represents the ion flux, D_i is the diffusivity, v_i is the ion mobility, z_i is the ion valence, F is Faraday's constant, and ϕ is the electrostatic potential. The subscript $i = 1$ corresponds to H^+ .

The electrostatic potential ϕ is determined by the local free charge density, as described by the Poisson equation:

$$-\varepsilon_0 \varepsilon_r \nabla^2 \phi = \rho_e \quad (3)$$

$$\rho_e = F \sum z_i c_i \quad (4)$$

where ρ_e is the local free charge density, ε_0 is the vacuum permittivity, and ε_r is the relative permittivity of the solution.

The flow field \mathbf{u} is described by the Stokes equation:

$$-\nabla p + \eta \nabla^2 \mathbf{u} - \rho_e \nabla \phi = 0 \quad (5)$$

$$\nabla \cdot \mathbf{u} = 0 \quad (6)$$

where p is the pressure and $\rho_e \nabla \phi$ represents the electrical body force resulting from the coupling between the charge density and the electric field.

Chemical reactions are modeled using boundary conditions that define the molar proton fluxes on the motor surface. The motor has a uniform zeta potential, $\phi = \zeta_m$, and moves parallel to the bottom wall with a velocity V . The boundary conditions on the motor surface are as follows:

$$\mathbf{n} \cdot \mathbf{J}_{i,\text{cathode}} = -J \delta_{i,1} \quad \text{if } -\beta_- < \beta < \beta_- \quad (7)$$

$$\mathbf{n} \cdot \mathbf{J}_{i,\text{anode}} = J_a \delta_{i,1} \quad \text{if } -\beta_- - \beta_+ < \beta < -\beta_- \text{ or } \beta_- < \beta < \beta_- + \beta_+ \quad (8)$$

$$\mathbf{n} \cdot \mathbf{J}_i = 0 \quad \text{otherwise} \quad (9)$$

$$\phi = \zeta_m \quad (10)$$

$$\mathbf{u} = V \mathbf{e}_x \quad (11)$$

where β is the azimuthal angle as defined in the Figure S11, and β_+ and β_- represent the anode and cathode regions, respectively. The proton flux on the anode, J_a , is set to $J \beta_- / \beta_+$, ensuring that the net ion flux is zero. In the calculation, we set $\beta_+ = 32^\circ$ and $\beta_- = 85^\circ$.

At the wall, the chemical fluxes are zero, the zeta potential is $\phi = \zeta_w$, and the no-slip boundary condition is applied:

$$\mathbf{n} \cdot \mathbf{J}_i = 0 \quad (12)$$

$$\phi = \zeta_w \quad (13)$$

$$\mathbf{u} = 0 \quad (14)$$

The hydrodynamic stress tensor σ_H and the Maxwell stress tensor σ_E are derived from the physical fields as:

$$\sigma_H = p \mathbf{I} + \eta (\nabla \mathbf{u} + (\nabla \mathbf{u})^T) \quad (15)$$

$$\sigma_E = \varepsilon (\mathbf{E} \mathbf{E} - \frac{E^2}{2} \mathbf{I}) \quad (16)$$

where \mathbf{E} is the electric field and \mathbf{I} is the identity matrix. The force and torque exerted on the motor

due to the chemical reaction are calculated as:

$$F_x = \mathbf{e}_x \cdot \oint_{\text{motor}} (\sigma_E + \sigma_H) \cdot d\mathbf{S} \quad (16)$$

$$F_z = \mathbf{e}_z \cdot \oint_{\text{motor}} (\sigma_E + \sigma_H) \cdot d\mathbf{S} \quad (16)$$

$$T_y = \oint_{\text{motor}} (\mathbf{r} - \mathbf{r}_0) \times (\sigma_E + \sigma_H) \cdot d\mathbf{S} \quad (16)$$

where \mathbf{r} represents points on the motor surface, \mathbf{r}_0 is the center of the motor, and $d\mathbf{S}$ is the surface element with unit normal vector \mathbf{n} .

The total force and torque applied to the motor is given by:

$$F_{\text{tot},x} = F_x \quad (12)$$

$$F_{\text{tot},z} = F_z - F_g \quad (13)$$

$$T_{\text{tot}} = T_y - T_g \cos \theta \quad (14)$$

In this steady-state model, the total force and torque are set to zero. The 5 μm motor moves near a charged wall at a constant self-propelling speed V , with a tilt angle θ and a height h . We use an iterative method^[1] to satisfy these balance conditions, resulting in typical motor parameters near the wall: $\theta = 11.5^\circ$, $h = 0.27 \mu\text{m}$, and $V = 3.1 \mu\text{m/s}$. When a specific parameter is queried, the other balance parameters are fixed.

Unless stated otherwise, the parameters used in this study are listed in Table S1. The zeta potentials ζ_m , ζ_w , and flux values are determined based on Refs.^[4-7], with the proton flux further adjusted to match the experimental self-propelling speed. The diffusivities of background ions BI^+ and BI^- are assumed to be the same as those of K^+ and Cl^- . The bulk concentration $c_{\text{bulk},i}$ is determined by the Debye length, which is estimated from the motor height.

We also present the physical fields around the motor at steady-state. In Figure S12, we plot spatial distributions of protons concentration c_1^* , the electric potential ϕ^* and flow field \mathbf{u} around a sliding motor. For clarity, we remove the sharp changes of fields in the Debye layer by subtracting background fields in the absence of chemical reactions from instantaneous fields, noted with asterisk superscript.

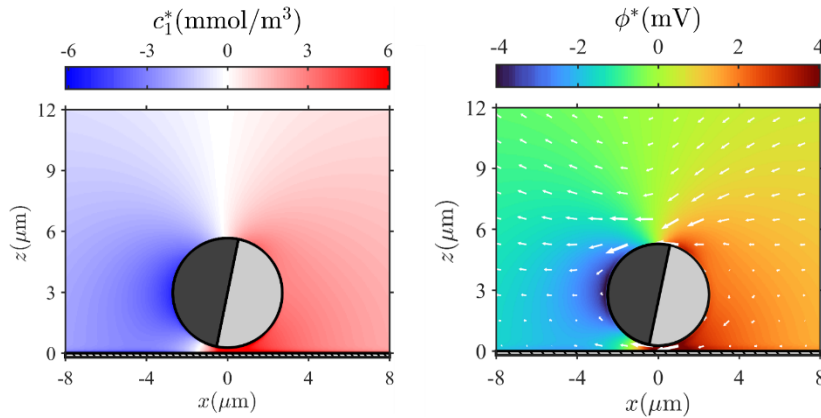


Figure S12. Instantaneous fields of hydrogen ion concentration c_1^* and electric potential ϕ^* around a Janus motor near a flat wall. These fields represent the values after subtracting those obtained in the absence of proton flux. The white arrows indicate the distribution of the fluid flow field.

Table S1. Parameters used for COMSOL modeling.

parameter	value	parameter	value
r	2.5 μm	T	293.15 K
ζ_w	-0.05 V	η	1.003×10^{-3} Pa·s
ζ_m	-0.04 V	$z_{1,3}$	1
ϵ_0	8.85×10^{-12} C/(V·m)	$z_{2,4}$	-1
ϵ_r	80	D_1	9.31×10^{-9} m ² /s
β_-	85°	D_2	5.03×10^{-9} m ² /s
β_+	32°	D_3	1.957×10^{-9} m ² /s
J	2.0×10^{-5} mol/(m ² ·s)	D_4	2.032×10^{-9} m ² /s
F_g	0.16 pN	$c_{\text{bulk } 1,2}$	3.5×10^{-6} mol/L
T_g	1.0 pN $\times\mu\text{m}$	$c_{\text{bulk } 3,4}$	1.6×10^{-5} mol/L

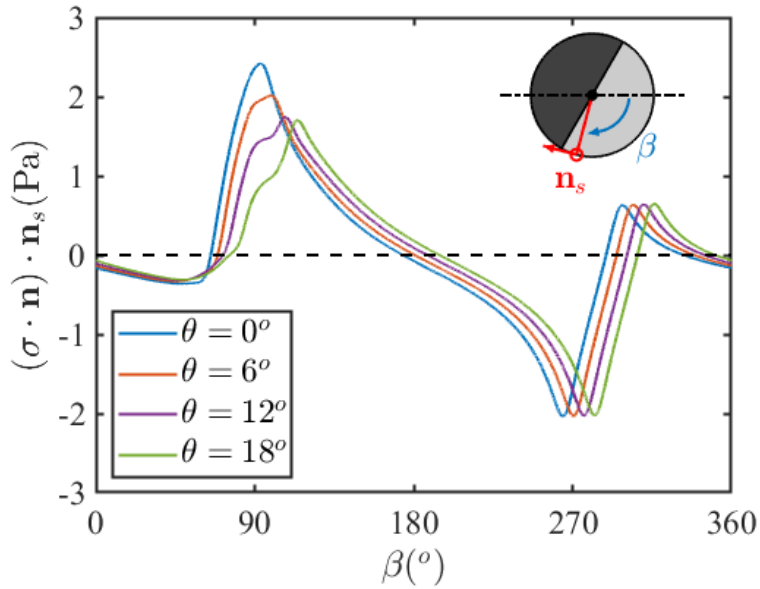


Figure S13. Hydrodynamic stress calculated at different points of a Pt Janus colloid for different tilt angles. The tangential hydrodynamic stress $\sigma \cdot \mathbf{n}_s$ is calculated as a function of azimuthal angle (β , see inset for definition), where the unit tangential vector is defined as $\mathbf{n}_s = (-\sin\beta, -\cos\beta)$, following a clockwise positive convention. The results reveal that electroosmotic flow stress near the boundary ($\beta \approx 90^\circ$) significantly decreases as the active colloid tilts its PS cap toward the wall (i.e. increasing θ), whereas the stress on the opposite side ($\beta \approx 270^\circ$) remains largely unaffected. Consequently, T_A decreases with increasing tilt angle and eventually becomes negative, explaining the observed sign change around $\theta \approx 13\text{--}14^\circ$ in Figure 4b in the main text.

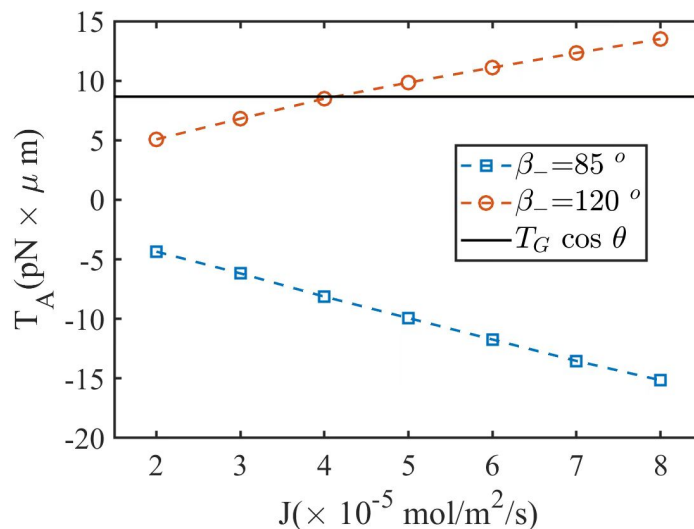


Figure S14. Activity-induced torque (T_A) values simulated for different chemical flux on the Pt cap (J) at two cap coverage values (β_- , the azimuthal angle for the cathodic part of the Pt cap, see Fig. S11 for definition). The θ of the sphere is fixed at 30° , which is a large value specifically chosen to find the simulation parameters necessary to allow such a large tilt. The results show that T_A values calculated at $\beta_- = 85^\circ$ are increasingly negatively at increasing J , so that a steady state θ where $T_A + T_G = 0$ cannot be found. Rather, increasing $\beta_- = 120^\circ$ reversed the sign of T_A and a steady state θ is found at $J \approx 4 \times 10^{-5} \text{ mol}/(\text{m}^2 \cdot \text{s})$. The values of β_+ are the same for these two cases.

Reference

- (1) Xu, Y.; Liu, C.; Liu, J.; Xu, P.; Xiao, Z.; Wang, W.; Zhang, H. P. Measuring Attractive Interaction between a Self-Electrophoretic Micromotor and a Wall. *Physical Review Letters* **2024**, *133* (25), 258304. DOI: 10.1103/PhysRevLett.133.258304.
- (2) Lyu, X.; Liu, X.; Zhou, C.; Duan, S.; Xu, P.; Dai, J.; Chen, X.; Peng, Y.; Cui, D.; Tang, J.; et al. Active, Yet Little Mobility: Asymmetric Decomposition of H₂O₂ Is Not Sufficient in Propelling Catalytic Micromotors. *Journal of the American Chemical Society* **2021**, *143* (31), 12154-12164. DOI: 10.1021/jacs.1c04501.
- (3) Ketzetzi, S.; de Graaf, J.; Kraft, D. J. Diffusion-Based Height Analysis Reveals Robust Microswimmer-Wall Separation. *Physical Review Letters* **2020**, *125* (23), 238001. DOI: 10.1103/PhysRevLett.125.238001.
- (4) Wang, W.; Chiang, T.-Y.; Velegol, D.; Mallouk, T. E. Understanding the Efficiency of Autonomous Nano- and Microscale Motors. *Journal of the American Chemical Society* **2013**, *135* (28), 10557-10565. DOI: 10.1021/ja405135f.
- (5) Moran, J. L.; Wheat, P. M.; Posner, J. D. Locomotion of electrocatalytic nanomotors due to reaction induced charge autoelectrophoresis. *Physical Review E* **2010**, *81* (6), 065302. DOI: 10.1103/PhysRevE.81.065302.
- (6) Dougherty, G. M.; Rose, K. A.; Tok, J. B.-H.; Pannu, S. S.; Chuang, F. Y. S.; Sha, M. Y.; Chakarova, G.; Penn, S. G. The zeta potential of surface-functionalized metallic nanorod particles in aqueous solution. *ELECTROPHORESIS* **2008**, *29* (5), 1131-1139. DOI: <https://doi.org/10.1002/elps.200700448>.
- (7) Liu, C.; Zhou, C.; Wang, W.; Zhang, H. P. Bimetallic Microswimmers Speed Up in Confining

Channels. *Physical Review Letters* **2016**, *117* (19), 198001. DOI: 10.1103/PhysRevLett.117.198001.